

PAPER • OPEN ACCESS

Characteristics of ion beams generated in the interaction of ultra-short laser pulses with ultra-thin foils








To cite this article: A McIlvenny *et al* 2020 *Plasma Phys. Control. Fusion* **62** 054001

View the [article online](#) for updates and enhancements.

You may also like

- [Review of laser-driven ion sources and their applications](#)
Hiroyuki Daido, Mamiko Nishiuchi and Alexander S Pirozhkov
- [Multi-species ion acceleration from sub-ps, PW interactions with ultra-thin foils](#)
O McCusker, H Ahmed, A McIlvenny et al.
- [Fast ignition with laser-driven proton and ion beams](#)
J.C. Fernández, B.J. Albright, F.N. Beg et al.

Characteristics of ion beams generated in the interaction of ultra-short laser pulses with ultra-thin foils

A McIlvenny¹ , H Ahmed¹, C Scullion¹, D Doria^{1,2} , L Romagnani^{1,3},
P Martin¹, K Naughton¹, A Sgattoni⁴ , D R Symes⁵, A Macchi^{4,6} ,
P McKenna⁷ , M Zepf^{1,8}, S Kar¹  and M Borghesi¹ 

¹ Centre for Plasma Physics, Queen's University Belfast, University Road BT71NN, United Kingdom

² Extreme Light Infrastructure—Nuclear Physics (ELI-NP), Horia Hulubei Institute for Nuclear Physics (IFIN-HH), Romania

³ LULI, École Polytechnique, CNRS, Route de Saclay, F-91128 Palaiseau Cedex, France

⁴ CNR/INO (National Institute of Optics), Adriano Gozzini unit, I-56124 Pisa, Italy

⁵ Central Laser Facility, Rutherford Appleton Laboratory, Oxfordshire OX11 0QX, United Kingdom

⁶ Enrico Fermi Department of Physics, University of Pisa, largo Bruno Pontecorvo 3, I-56127 Pisa, Italy

⁷ SUPA, Department of Physics, University of Strathclyde, Glasgow G4 0NG, United Kingdom

⁸ Helmholtz Institute Jena, Fröbelstieg 3, D-07743 Jena, Germany

E-mail: amcilverny01@qub.ac.uk and m.borghesi@qub.ac.uk

Received 6 December 2019, revised 26 February 2020

Accepted for publication 5 March 2020

Published 30 March 2020



CrossMark

Abstract

Experiments investigating ion acceleration from laser-irradiated ultra-thin foils on the GEMINI laser facility at the Rutherford appleton laboratory indicate a transition to 'light sail' radiation pressure acceleration when using circularly polarised, high contrast laser pulses. This paper complements previously published results with additional data and modelling which provide information on the multispecies dynamics taking place during the acceleration, and provides an indication on expected scaling of these processes at higher laser intensities.

Keywords: radiation pressure, ion-acceleration, laser-plasma accelerator

(Some figures may appear in colour only in the online journal)

1. Introduction

Amongst several applications of intense laser matter interactions, laser-driven ion acceleration has attracted very significant attention, motivated by a broad range of possible applications [1]. Most work so far has studied ions generated by the well established target normal sheath acceleration (TNSA) mechanism, which typically employs micron-thick targets and generate beams with unique characteristics in terms of ultra-short (ps) duration (at the source) and extreme laminarity [1–3]. A different acceleration mechanism,

radiation pressure acceleration (RPA), can in principle produce ion beams with even more beneficial properties for applications, such as smaller divergence, narrow energy spread and high conversion efficiency, particularly in the light-sail (LS) regime. With ongoing progress in high power laser technology, intensities above 10^{22} W cm⁻² will soon be routinely available, where this mechanism is predicted to dominate as suggested via a number of numerical studies [4–8], with other work suggesting approaches for entering this regime at currently attainable intensities [9, 10]. The ultra-short pulse (<100 fs) regime is of particular interest due to the potential to move to high-repetition rate, an important requirement for future laser-driven accelerators.

Interactions of high intensity, ultra-short (40 fs) laser pulses with ultra-thin (10–100 nm carbon) foils are typically characterised by efficient acceleration of higher Z ions from



Original content from this work may be used under the terms of the [Creative Commons Attribution 4.0 licence](https://creativecommons.org/licenses/by/4.0/). Any further distribution of this work must maintain attribution to the author(s) and the title of the work, journal citation and DOI.

the target bulk, e.g. C^{6+} when employing carbon foils, in addition to protons. Employing circular rather than linear polarisation (LP) and irradiating at normal incidence in these interactions, has, in principle, the advantage of a reduced electron heating (by removing the oscillating component of the ponderomotive force), which has the effect of mitigating relativistic transparency and allowing radiation pressure to be applied to the target for longer [4]. Experimentally, this needs to be coupled to pulse contrast enhancement, typically by using a double plasma mirror (DPM), so that the integrity of the target can be preserved up to the high intensity interaction. A number of experiments has tested the beneficial use of circular polarisation (CP) on the acceleration of the bulk ions, by either directly irradiating ultra-thin foils [11, 12], or by exploiting relativistic pulse-shaping in a near-critical plasma preceding the foil [13, 14]. Under optimised conditions, the energy per nucleon of these heavier ions can become comparable to the energy of the protons. In the work reported in [12], in addition to the polarisation dependence, we observed a strong dependence of the characteristics of the accelerated ions on the target thickness. For the thicker targets (50–100 nm), the maximum ion energies were higher for pulses with LP, while, below 25 nm, significantly higher energies for both carbon ions and protons were observed when CP was utilised, reaching a maximum of 25 and 33 MeV/nucleon respectively for 10 nm targets. With the support of particle in cell (PIC) simulation, these results were highlighted in [12] as the indication of a transition to the LS-RPA regime.

Indeed, the LS-RPA process is strongly dependent on laser and target parameters with the ion energy per nucleon (E_{ion}) scaling as:

$$E_{ion} \propto \left(\frac{a_0^2 \tau_{LS}}{\chi} \right)^2, \quad (1)$$

where a_0 is the laser's normalised vector potential, τ_{LS} is the pulse length and $\chi = \frac{\rho L}{\lambda m_p n_c}$ where ρ is the mass density, m_p is the mass of the proton, L is the target thickness and n_c is the critical density [15]. For a given target density, the existence of an optimal thickness (ℓ) for efficient LS acceleration is predicted analytically [6], through the condition $a_0 = \pi \frac{n_e \ell}{n_c \lambda}$ where n_e is the electron density and λ is the laser wavelength. For the conditions in [12] i.e. $I \approx 6 \times 10^{20} \text{ W cm}^{-2}$, $a_0 \approx 13$, $n_e = 350 n_c$, where $a_0 = \frac{0.85}{\sqrt{2}} \sqrt{I \lambda^2 / (10^{18} \text{ W cm}^{-2}) (\mu\text{m}^2)}$ for a CP pulse, the optimal thickness is calculated to be ≈ 10 nm.

Tight focusing of the laser beam, leading to strongly non-homogeneous irradiation across the focal spot can limit the efficiency of the laser-target coupling by causing excessive electron heating radially from the focal spot, as the laser is no longer normal to the deformed target. Multi-dimensional simulations have also shown the effects of a strong RPA drive producing Rayleigh–Taylor instabilities [16] and subsequent target break up [17]. Deviations from ideal conditions, as determined by these detrimental effects, can have a significant effect on the maximum ion energies produced by RPA, for example through an early onset of target transparency which

terminates the RPA phase. Nevertheless, entering into the relativistically induced transparency regime (RIT) can also lead, under appropriate conditions, to direct laser heating of electrons and enhanced acceleration of protons [18, 19].

This paper presents further experimental results obtained in the campaign reported in [12] detailing species-resolved ion energy spectra as well as the ion beam profiles generated from the various regimes accessed with the different target and laser parameters. This is compared to multi-dimensional PIC simulations which provide further insight into the dynamics of the interaction as well as the dependence on target thickness and laser polarisation. Extending these numerical simulations matching the experimental results, we extrapolate our considerations to predict what ion energies one may expect when applying short pulse PetaWatt systems to this interaction regime.

2. Experimental set up

The experiment was carried out on the ASTRA GEMINI Ti:sapphire laser system at the Rutherford Appleton Laboratory, STFC, UK. The laser delivered up to ~ 6 J energy on target in pulses of 40 fs duration at full width half maximum (FWHM), with a central wavelength of 800 nm, after being reflected off a DPM to temporally clean the pulse, producing a relative intensity contrast of 10^{-6} at 1 ps before the pulse. The laser beam, re-collimated after the plasma mirrors, was focused onto the targets at normal incidence by an $f/2$ off-axis parabolic mirror, delivering peak intensities on target $\sim 6 \times 10^{20} \text{ W cm}^{-2}$. The laser polarisation was varied by employing a zero order quarter wave plate, placed between the second plasma mirror and the focusing parabola. A schematic of the set-up can be seen in figure 1 of [12].

Amorphous carbon targets with thickness (L), in the range 10–100 nm were irradiated. The energy spectra of the ions generated from the interaction were resolved by the use of a Thomson parabola spectrometer (TPS) along the laser axis (also target normal axis) with an acceptance angle of $1.1 \mu\text{Sr}$. The TPS employed BAS-TR image plate, calibrated to provide the absolute particle number [20, 21]. The TPS samples a small portion of the beam in order to accurately resolve each species and their energy spectra. To complement these measurements, energy-resolved spatial profiles of the ion beam were recorded by using stacks of radiochromic (RCF) and CR-39 detectors on dedicated shots. Two types of RCF were used in the stack, HD-V2 and EBT2, as their different sensitivity allowed us to diagnose the proton beam over the large variations in particle density present across the spectrum [22].

3. Experimental results and comparison with simulations

Experimental results provided evidence of a transition to LS acceleration when moving to the thinnest targets (10 nm) and employing CP. Figure 1 shows the maximum energies for

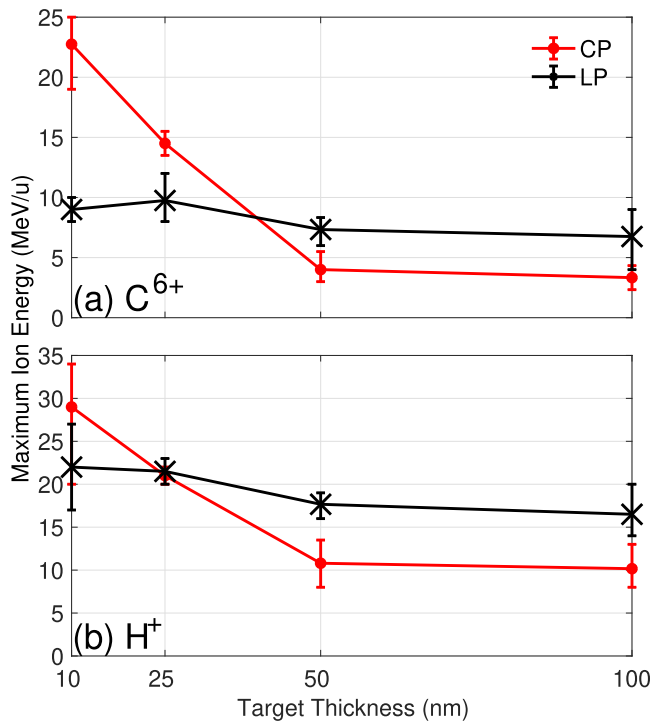


Figure 1. Average maximum ion energy measured from the TPS. A target thickness scan showing maximum ion energies for (a) C^{6+} and (b) protons for LP and CP is displayed. Error bars represent the shot to shot variation over 3 shots, with the exception of the 10 nm thickness where 4 shots are considered for LP and 6 for CP (including 3 from RCF data for protons).

C^{6+} and protons obtained in the experiment, as a function of target thickness and polarisation. It can be seen that CP results in higher energies for C^{6+} for targets thinner than 50 nm up to a maximum of 25 MeV/u for 10 nm foils, a six-fold increase in energy compared to that obtained for 100 nm (4 MeV/u), with only a slight increase observed at 25 nm. Protons show a similar trend with higher energies for CP for the thinnest targets, reaching a maximum of 33 MeV at 10 nm. The average value for at least 3 shots is plotted with error bars representing the shot to shot variation; additional information on the proton cut-off was retrieved for 10 nm targets from dedicated shots on RCF.

An increase in both proton and C^{6+} energies with decreasing thickness would be expected, in a Light Sail scenario, owing to the reduced target areal density in equation (1). For LP, a similar, more modest, increase is seen for both ion species at 10–25 nm, with the energy per nucleon remaining much higher for protons across the whole range of thicknesses. This suggests that the increased electron heating and enhanced sheath field acceleration in a RIT regime as the dominant factors at work [18]. This trend is consistent with other work for similar target thicknesses and exploring the transition from TNSA to transparency [23].

The ion spectra also indicate bulk acceleration consistent with an RPA regime; for CP the C^{6+} (figure 2(a)) shows the presence of spectral peaks for thick targets which move to higher energies for the thinner targets albeit with a larger energy spread. This spectral enhancement, compared to LP,

can be attributed to the reduced electron heating allowing a sustained bulk acceleration via RPA as initially discussed experimentally in [11].

The interplay of different acceleration mechanisms can also be inferred from the proton beam profiles obtained from RCF stacks and their comparison with 3D simulations (figure 3). 3D simulations were performed using the ALaDyn code [24, 25] for the 10 nm foil for CP and LP with further 2D simulations performed in EPOCH [26] to explore different target thicknesses (the reduced dimensionality was used due to the large computational requirements for running 3D simulations). The 3D simulation grid was initialised as $6144 \times 2048 \times 2048$ (x (laser direction), y , z), with a grid resolution of $\Delta x = 8.3$ nm, $\Delta y = \Delta z = 4\Delta x$ which is stretched towards the edges to reduce the computational cost with a moving window in the x direction. To further optimise the computational load, the 10 nm target was initialised as being thicker (but with lower density) as a neutralised 35 nm C^{6+} foil with a peak density of $100n_c$; this has an equivalent areal density to a 10 nm carbon foil of $350n_c$. This configuration helps to balance the computational workload across the available processors. The rear side contains a 12.5 nm hydrogen layer with $10n_c$ density, representative of the contaminant layer; this configuration was chosen for the 3D simulations to reduce the computational cost of additional particles required for front surface protons since 2D simulations show that the multi-species dynamics are similar whereby front protons quickly ‘overtake’ the carbon and co-move with the rear surface protons.

Follow-up 2D simulations were performed on a fixed grid of 8000×3000 ($\Delta x = \Delta y = 5$ nm) and 200 particles per cell per species. The target was equally initialised as in the 3D case. The laser had a peak intensity of 5.5×10^{20} W cm⁻², 3 μ m FWHM Gaussian focal spot and 40 fs FWHM Gaussian pulse duration, representative of the Gemini irradiation conditions. The 2D and 3D simulations produce ion energies within 20% of each other, and present the same trend of ion energy as a function of laser polarisation [12].

The proton beam profile in the simulations can be directly compared to the experimental RCF data by selecting particles with the same energy and plotting their Y and Z positions; this projection will then be representative of the flux distribution on an RCF layer. The RCF layers measuring proton energies of 10 and 20 MeV for circularly polarised pulses are displayed (figures 3(a) and (c) respectively), alongside the equivalent result from simulations (figures 3(b) and (d)). The equivalent RCFs for LP (figures 3(e) and (g)) are also shown alongside the corresponding numerical result (figures 3(f) and (h)).

At low energies (<10 MeV), a ring like structure is observed in the beam for CP whereas for higher energies, which result from the RPA phase, the profile is quite different displaying a bubble structure, similar to patterns attributed, in previous numerical and simulation work [16, 17, 27], to be the effect of Rayleigh Taylor Instabilities as the radiation pressure acts on the critical density surface, and shown experimentally in [17, 28]. The signal on the 10 MeV layer for CP is assumed to be from protons since, although high

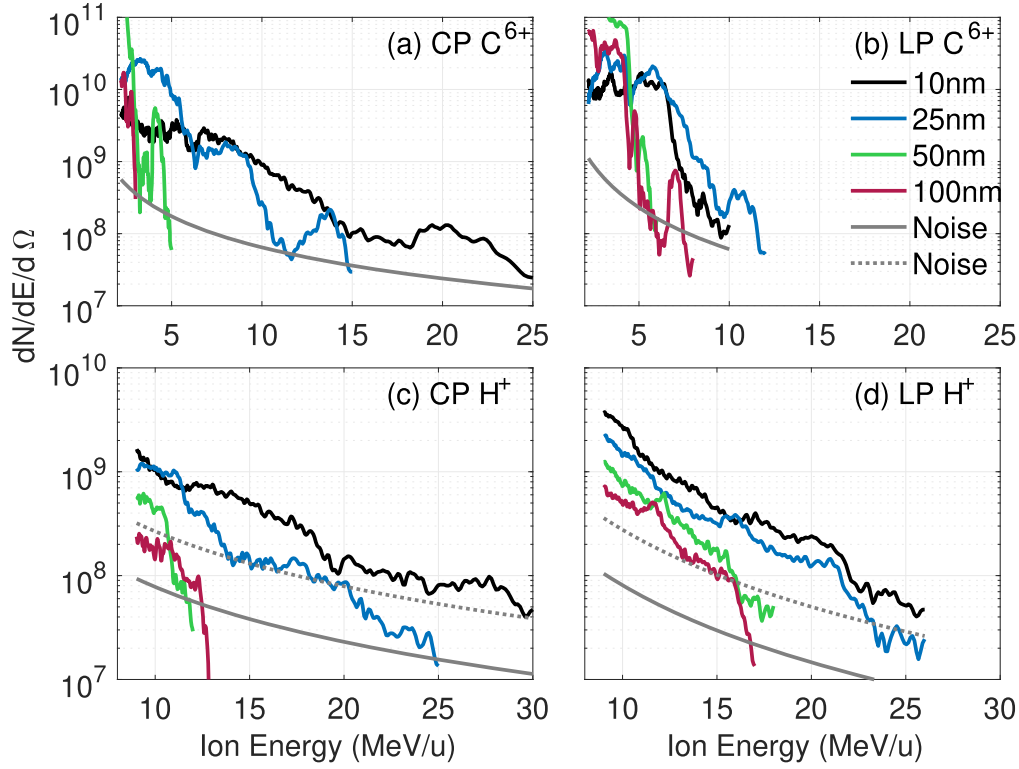


Figure 2. Energy spectra for CP (left) and LP (right) for C^{6+} (top) and H^+ (bottom). Solid grey line represents the typical noise. For shots with higher noise, e.g. 10 nm H^+ , an additional dotted grey line is added as a better representation.

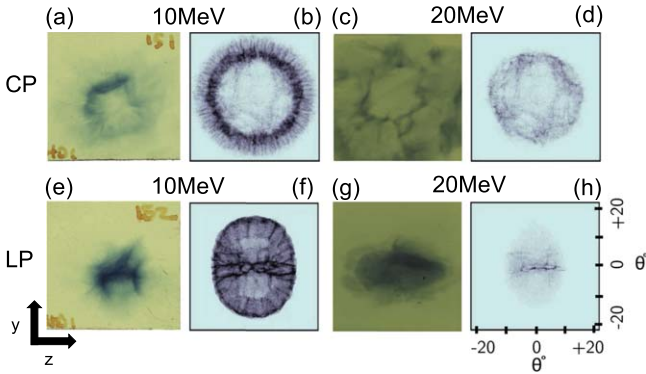


Figure 3. CP (a)–(d) and LP (e)–(h) proton beam profiles at 10 MeV (left) and 20 MeV (right) obtained experimentally from RCF (a), (c), (e), (g) and through 3D PIC simulations (b), (d), (f), (h). Note the ellipse in (g), with the major axis (in z -direction) aligned to the laser polarisation direction. All images represent the same solid angle of the beam profile (marked in h).

energy carbon (>20 MeV/ u) will also penetrate to this depth in the RCF stack, simulations indicate that the C^{6+} ions produce a more directional beam along the laser axis thus not contributing to this ‘ring’ profile.

Figure 4 displays the maximum C^{6+} ion energy versus time in the 3D simulations plotted together with the analytical prediction of ion energies in the LS regime for a Gaussian laser pulse [29]:

$$\beta = \frac{v_{LS}}{c} = \frac{[(1 + \epsilon(t))^2 - 1]}{[(1 + \epsilon(t))^2 + 1]}, \quad (2)$$

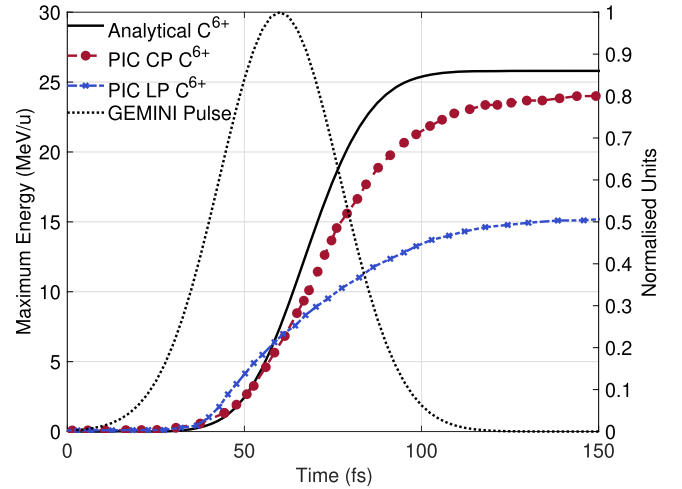


Figure 4. Energy of C^{6+} with time for a modelled Gaussian laser fluence for the RPA-LS regime from equation (3) (solid black) representative of the Gemini pulse (dotted black, right axis) along with the maximum energy (left axis) from 3D simulations for CP (red dashed) and LP (blue dotted).

where

$$\epsilon(t) = \frac{2F(t)}{\rho L c^2} \quad (3)$$

with $F(t)$ the fluence at time t , and ρL (density times thickness) the areal density. In both simulations and analytical calculations, we assume $\rho = 362.5n_c$, and $L = 10$ nm. The ion energy per nucleon is calculated analytically as $E_{ion} = m_p c^2 (\gamma - 1)$ where

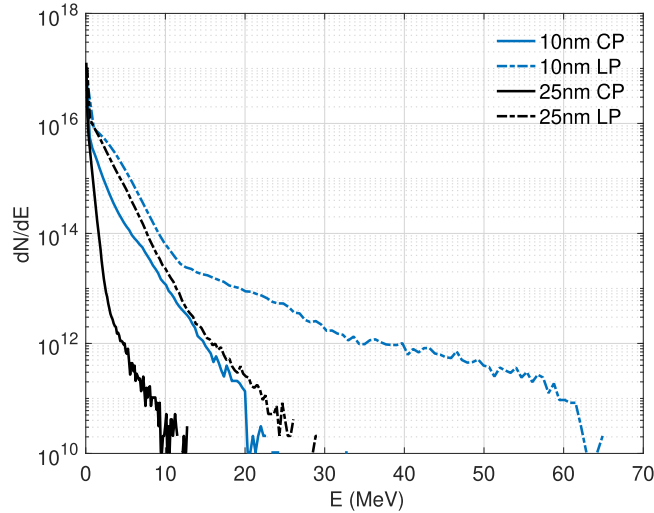


Figure 5. Angle-integrated electron spectra for two different target thickness (10 and 25 nm) for CP (solid line) and LP (dashed line) from 2D simulations at $t = t_0 + 35$ fs where t_0 is the peak of the pulse hitting the target.

$\gamma = (1 - \beta^2)^{-0.5}$ and m_p is the mass of the proton. The comparison supports the interpretation that the target bulk is initially accelerated by RPA in the LS regime until the target rarefies after the peak of the pulse, causing a de-coupling of the critical surface from the compressed LS electron layer. For LP, deviation from the analytical prediction take place much sooner due to the earlier onset of transparency.

To elaborate further on the dependence of the proton's spatial and spectral structure from target thickness and polarisation, the angular and spectral structure for three likely scenarios have been compared in 2D PIC simulations: 'thick' targets and TNSA; RPA for thin targets remaining opaque during the irradiation; acceleration in thin targets undergoing RIT. For 10 nm targets, a very significant difference in the electron temperature between LP and CP is observed at the end of the pulse (5 MeV and 1.2 MeV respectively, estimated by fitting the profiles shown in figure 5); as discussed in the previous section, electrons are strongly heated by the LP pulse due to $\mathbf{J} \times \mathbf{B}$ heating, resulting in the target undergoing RIT which further heats the electrons. This effect is delayed in the CP case, with the electron temperature remaining low as long as the target stays opaque.

The effect of the laser polarisation and target thickness on the proton beam profile can be also assessed from figure 6, where the beam profiles for H^+ are compared for CP and LP. For CP, a 'hole' in the centre of the beam persists in the spectrum at low and intermediate energies. Extrapolating this 2D information to a 3D geometry and assuming azimuthal symmetry, will result in a ring structure as seen in figure 3 for the CP case. The beam is heavily modulated and non-uniform at all energies in contrast to the LP case which produces a relatively smooth beam at all energies. This is likely due to the more uniform electron heating associated with direct laser acceleration and the absence of the instabilities associated with RPA.

Looking at the thicker targets (25 nm) in figure 6, apart from the differences in the maximum energy for the different polarisations, there are some noticeable variations in the angular distributions of the particles. For CP, there is no longer a 'hole'

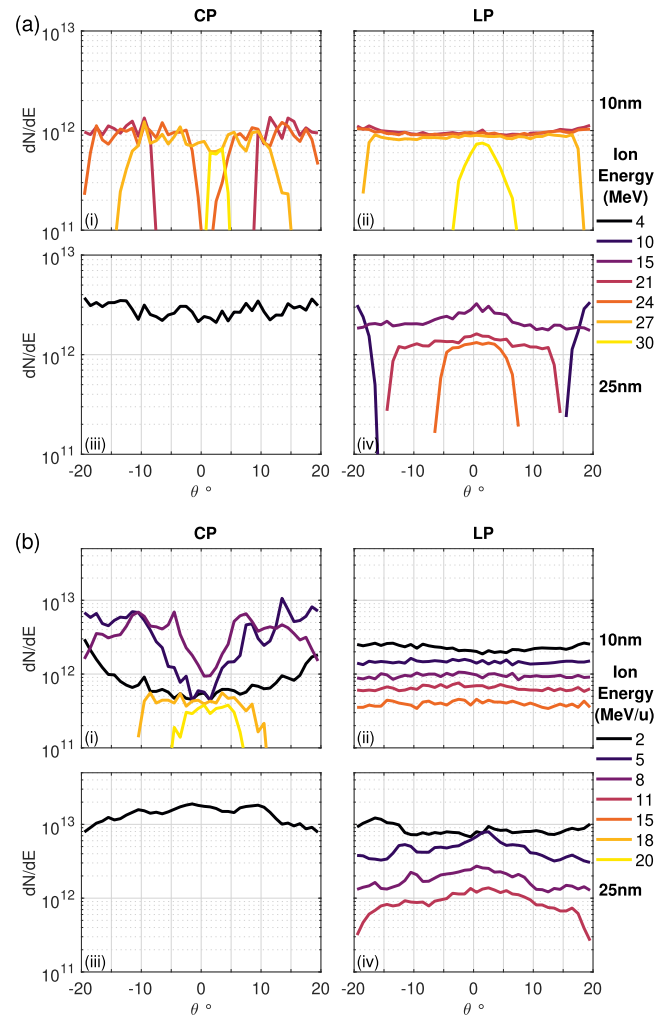


Figure 6. 2D ion angular distributions for (a) protons and (b) C^{6+} for (i) CP 10nm, (ii) LP 10nm, (iii) CP 25nm and (iv) LP 25nm at $t = t_0 + 100$ fs.

in the centre of the proton beam, as this target will not go transparent at all during the interaction nor do ions gain significant energy from RPA due to the above-optimal areal density. For LP, although the energy spectrum of the proton beam looks similar, the maximum proton energy is lower than for the 10 nm case. LP again results in a higher electron temperature as one would expect (1.8 MeV compared to 0.1 MeV respectively, according to figure 5). This, along with the reduced electron heating suggests that these particles are accelerated by a more uniform sheath field associated with TNSA. LP plots in figure 8 for 25 nm show a smoother E_x field than for 10 nm; however, it is also seen that the 10 nm target shows strong laser transmission providing an additional boost to proton energies compared to the opaque 25 nm target.

Comparing the CP case between figures 7 and 8, it is seen that the 10 nm case has resulted in a much more significant acceleration via RPA-LS, due to its lower areal density. The strong deformation from the 10 nm target also comes with the side effect of off-axis acceleration of protons due to the oblique interaction of the laser with some of the deformed target, as shown in figure 9.

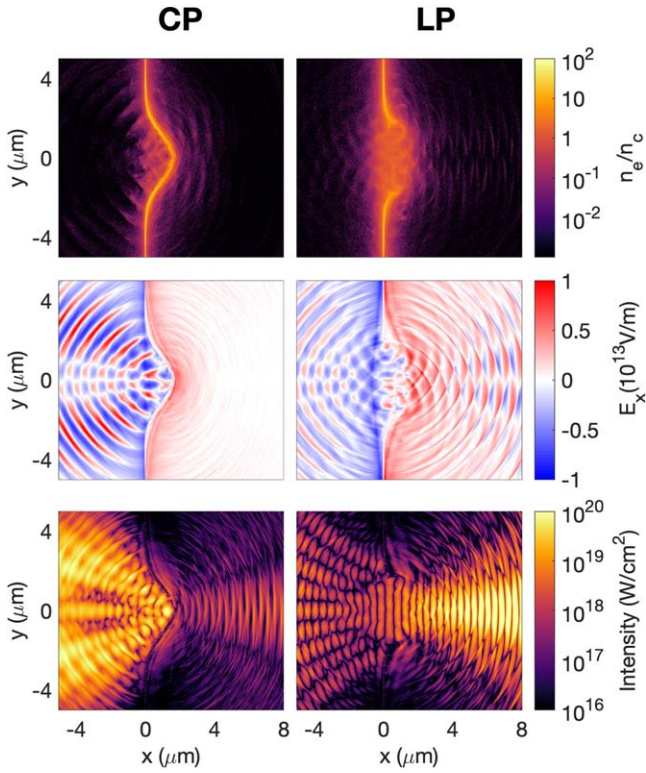


Figure 7. 2D PIC snapshots at $t = t_0 + 100$ fs. of electron density n_e (top), E_x (middle) and laser intensity (bottom) for CP (left) and LP (right) for a 10 nm target.

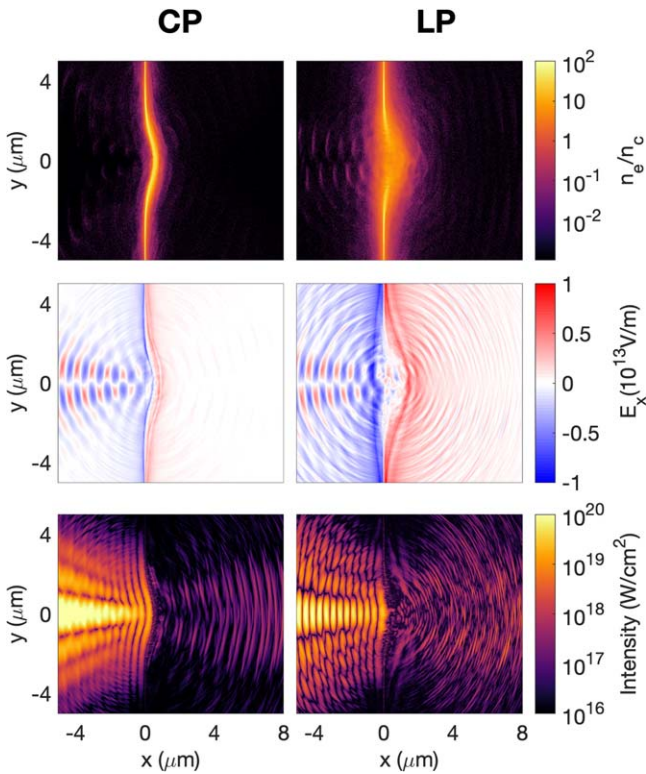


Figure 8. 2D PIC snapshots at $t = t_0 + 100$ fs. of electron density n_e (top), E_x (middle) and laser intensity (bottom) for CP (left) and LP (right) for a 25 nm target.

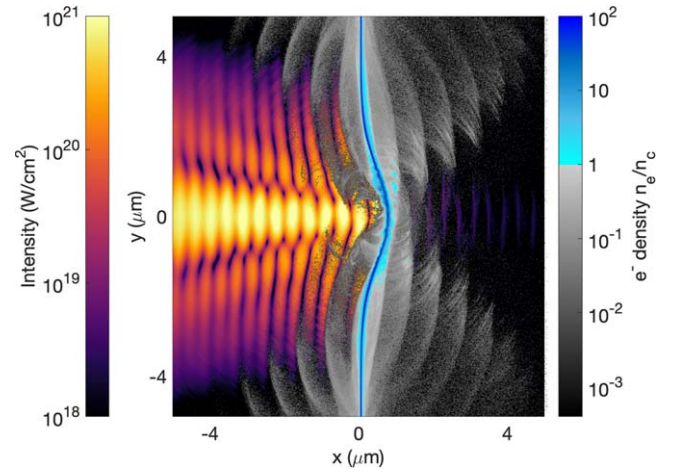


Figure 9. Electron density at the peak of the pulse (t_0), for CP, showing the cyclic electron heating off axis; the electron bunches are separated by one laser period indicating they are directly accelerated by the laser's electric field ($E^2 = E_y^2 + E_z^2$ for CP). The overdense layer is deformed by radiation pressure. The overdense electron density (blue) is shown along with the underdense (greyscale) plasma along with the intensity (left colour-scale).

The electron density is plotted in figure 9 normalised to the critical density along with the laser intensity; this shows that at the peak of the pulse, the electron layer remains overdense with no transmission. As the target deforms due to RPA, the rotating laser electric field vector will cyclically accelerate electrons off the laser axis in the direction of the local target normal. The spacing between the electron bunches corresponds to a laser period and alternates between the positive and negative y axis by half a period; by assuming azimuthal symmetry, we can infer that this produces a ring of electron bunches for circular polarisation. Hence the electrons get cyclically heated and protons are accelerated off axis by an electrostatic field as in TNSA. This results in the proton beam divergence in figure 9, where a 'hole' in the centre of the beam is also observed. Since the target has not gone transparent as in [27], the situation is more similar to work presented in [30] although with different experimental parameters.

4. Discussion

Moving on to the next generation of lasers where RPA processes are predicted to generate energies of clinical interest [5, 8], it is useful to estimate how the processes discussed so far will scale to higher intensities regimes so that appropriate plans can be made for experiments. The simulations presented earlier were repeated in EPOCH at higher intensities and at higher resolution to determine the scaling of the optimum thickness for LS-RPA, as well as of the maximum energy, versus intensity.

It has been discussed by Macchi *et al* [31] that the predicted I^2 scaling implied by equation (1) is only valid, for a fixed target thickness, as long as the target remains overdense. In reality, increasing the intensity will result in the target turning transparent during the interaction, which terminates LS acceleration. In order to avoid transparency, one has to therefore

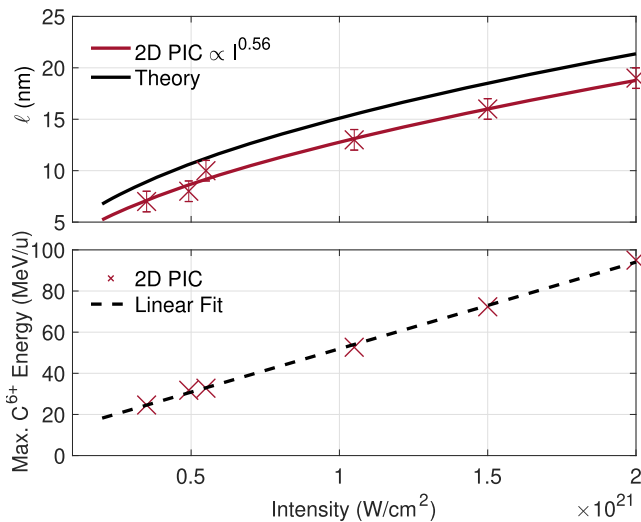


Figure 10. Optimum thickness (ℓ) and maximum carbon energy scaling with intensity. The optimum thickness scaling is overplotted with the best fit, $\ell \propto I^{0.56}$ and the maximum energy with a linear scaling. The pulse is 40 fs and 3 μm Gaussian FWHM.

increase the target thickness. Hence the optimum thickness changes with intensity which will also affect the maximum ion energy through the increase of the areal density. This has the effect of reducing the very fast I^2 scaling to a linear dependence as seen in figure 10. Here we focus on the acceleration of C^{6+} since this is accelerated from the target bulk while proton maximum ion energies are more likely to be affected, as discussed previously, by sheath acceleration mechanisms.

The scaling for the optimum thickness (ℓ) follows the same trend as the theoretical prediction given by:

$$\ell = \frac{a_0 \lambda n_c}{\pi n_e}, \quad (4)$$

where $a_0 \propto I^{1/2}$, and the rest of the terms have the usual meaning. The shift in optimal thickness between analytical estimate and numerical simulations is likely due to an earlier onset of transparency in 2D rather than predicted by a 1D theoretical approach.

These considerations suggest that, by scaling the laser energy up to achieve 1 PW of laser power (while keeping the pulse duration and focal spot size constant, at the values of our GEMINI experiment) we can expect to generate energies exceeding 66 MeV/u (0.8 GeV) for carbon ions. In principle this scaling could be extended further, e.g. until radiation reaction effects start being important.

Additional simulations (not shown here) indicate that increasing the laser intensity by focusing the laser pulse more tightly, e.g. by employing $f/1$ rather than $f/2$ optics leads to a much slower scaling and less effective acceleration, in broad agreement with the observations of [32].

5. Conclusion

We have presented experimental data on ion acceleration from ultra-thin foils irradiated by the intense GEMINI laser

pulse, which indicates a transition to LS acceleration with presently available laser intensities facilitated by the use of high contrast, circularly polarised pulses. Simulations confirm the advantage of reduced electron heating when utilising CP, which helps in maintaining target opacity during the laser irradiation, a necessary condition for the efficient application of the radiation pressure. In addition to reproducing the experimental trends for ion energies versus target thickness and laser polarisation, the simulations were also in qualitative agreement with the experiment in terms of proton beam profiles, and help clarifying the multispecies dynamics during the acceleration. By extrapolating the numerical simulations to higher intensities, on the basis of our experimental results, one predicts energies up to 70 MeV/u with 1 PW and a linear scaling of Carbon energies with intensities, in the intensity range that will be possible to explore in the very near future.

Acknowledgments

Authors would like to thank the support of technical staff at the GEMINI laser facility at STFC Rutherford Appleton laboratory as well as the target fabrication group. The work was funded by EPSRC grants EP/K022415/1, EP/J003832/1, EP/J50094/1 with EPOCH funded by grants EP/G056803/1, EP/G055165/1 and EP/M022463/1. ALaDyn simulations were performed on 16 384 BlueGene/Q cores on FERMI at CINECA (Bologna, Italy). EPOCH simulations were performed using computing resources provided by STFC Scientific Computing Department's SCARF cluster as well as the Kelvin HPC cluster at Queen's University Belfast. Data is available from [10.17034/bf77458d-25ac-49ab-a98b-a3461ec34b40](https://doi.org/10.17034/bf77458d-25ac-49ab-a98b-a3461ec34b40).

ORCID iDs

A McIlvenny <https://orcid.org/0000-0002-1044-1534>
 D Doria <https://orcid.org/0000-0001-8776-5791>
 A Sgattoni <https://orcid.org/0000-0003-0284-1690>
 A Macchi <https://orcid.org/0000-0002-1835-2544>
 P McKenna <https://orcid.org/0000-0001-8061-7091>
 S Kar <https://orcid.org/0000-0002-9406-3103>
 M Borghesi <https://orcid.org/0000-0001-9165-0073>

References

- [1] Macchi A, Borghesi M and Passoni M 2013 *Rev. Mod. Phys.* **85** 751–93
- [2] Daido H, Nishiuchi M and Pirozhkov A S 2012 *Rep. Prog. Phys.* **75** 056401
- [3] Schreiber J, Bolton P R and Parodi K 2016 *Rev. Sci. Instrum.* **87** 071101
- [4] Macchi A, Cattani F, Liseykina T V and Cornolti F 2005 *Phys. Rev. Lett.* **94** 165003
- [5] Esirkepov T, Borghesi M, Bulanov S V, Mourou G and Tajima T 2004 *Phys. Rev. Lett.* **92** 175003

- [6] Macchi A, Veghini S and Pegoraro F 2009 *Phys. Rev. Lett.* **103** 085003
- [7] Qiao B, Zepf M, Borghesi M and Geissler M 2009 *Phys. Rev. Lett.* **102** 145002
- [8] Bulanov S V, Echkina E Y, Esirkepov T Z, Inovenkov I N, Kando M, Pegoraro F and Korn G 2010 *Phys. Rev. Lett.* **104** 135003
- [9] Robinson A P L, Zepf M, Kar S, Evans R G and Bellei C 2008 *New J. Phys.* **10** 013021
- [10] Qiao B, Kar S, Geissler M, Gibbon P, Zepf M and Borghesi M 2012 *Phys. Rev. Lett.* **108** 115002
- [11] Henig A *et al* 2009 *Phys. Rev. Lett.* **103** 245003
- [12] Scullion C *et al* 2017 *Phys. Rev. Lett.* **119** 054801
- [13] Bin J H *et al* 2015 *Phys. Rev. Lett.* **115** 064801
- [14] Ma W J *et al* 2019 *Phys. Rev. Lett.* **122** 014803
- [15] Kar S *et al* 2012 *Phys. Rev. Lett.* **109** 185006
- [16] Sgattoni A, Sinigardi S, Fedeli L, Pegoraro F and Macchi A 2015 *Phys. Rev. E* **91** 013106
- [17] Palmer C A *et al* 2012 *Phys. Rev. Lett.* **108** 225002
- [18] Higginson A *et al* 2018 *Nat. Commun.* **9** 724
- [19] Yin L, Albright B J, Bowers K J, Jung D, Fernández J C and Hegelich B M 2011 *Phys. Rev. Lett.* **107** 045003
- [20] Doria D *et al* 2015 *Rev. Sci. Instrum.* **86** 123302
- [21] Mančić A, Fuchs J, Antici P, Gaillard S A and Audebert P 2008 *Rev. Sci. Instrum.* **79** 073301
- [22] Scullion C *et al* 2016 *J. Instrum.* **11** C09020
- [23] Poole P L *et al* 2018 *New J. Phys.* **20** 013019
- [24] Benedetti C, Sgattoni A, Turchetti G and Londrillo P 2008 *IEEE Trans. Plasma Sci.* **36** 1790–8
- [25] Londrillo P, Benedetti C, Sgattoni A and Turchetti G 2010 *Nucl. Instrum. Methods Phys. Res. A* **620** 28–35
- [26] Arber T D *et al* 2015 *Plasma Phys. Control. Fusion* **57** 113001
- [27] Gonzalez-Izquierdo B *et al* 2016 *Nat. Commun.* **7** 12891
- [28] Gonzalez-Izquierdo B *et al* 2016 *Nat. Phys.* **12** 505–12
- [29] Gonzalez-Izquierdo B *et al* 2018 *Appl. Sci.* **8** 336
- [30] Padda H *et al* 2016 *Phys. Plasmas* **23** 063116
- [31] Macchi A, Sgattoni A, Sinigardi S, Borghesi M and Passoni M 2013 *Plasma Phys. Control. Fusion* **55** 124020
- [32] Dollar F *et al* 2012 *Phys. Rev. Lett.* **108** 175005